INTERNATIONAL JOURNAL FOR NUMERICAL METHODS IN FLUIDS, VOL. 7, 733–755 (1987)

FULLY DEVELOPED FLOW IN A CURVED PIPE OF ARBITRARY CURVATURE RATIO

W. Y. SOH* AND S. A. BERGER

Department of Mechanical Engineering, University of California, Berkeley, CA 94720, U.S.A.

SUMMARY

It is generally assumed in curved pipe flow analyses that the curvature ratio, δ, of the pipe is very small, in which case the flow depends on a single parameter, the Dean number. This is not the case if δ is not very small. To determine the importance of this effect we have numerically solved the full Navier–Stokes equations, in primitive variable form, for arbitrary values of δ. A factored ADI finite-difference scheme has been used, employing Chorin's artificial compressibility technique. The results show that the central-difference calculation on a staggered grid is stable, without adding artificial damping terms, due to coupling between pressure and velocity. A spatially variable time step is used with a fixed Courant number.

KEY WORDS Curved Pipe Flow Artificial Compressibility Method Dean Number Secondary Flow Effect of Curvature Ratio

1. INTRODUCTION

Fully developed viscous flow in a curved pipe of circular cross-section was studied theoretically first by Dean.[1,2] He showed that for small curvature ratio, defined by $\delta = a/L$, the flow depends only on the single parameter $K = 2\delta R_d^2$, first introduced by Dean and now called the Dean number. Here a is the radius of the pipe cross-section and L the radius of curvature of the pipe central axis; the parameter R_d is defined as $R_d = Ga^3/4\mu\nu$, where G is the constant pressure gradient maintaining the flow, μ the viscosity and ν the kinematic viscosity. McConalogue and Srivastava[3] showed formally that the flow in a curved pipe with small δ is characterized by a single parameter D, which is a variant of the Dean number and defined as $(Ga^2/\mu)\ (2a^3/\nu^2 L)^{1/2}$, and obtained a numerical solution for the range $96 < D < 600$. Greenspan[4] and Collins and Dennis[5] have carried out finite-difference solutions using vorticity–stream-function formulations for flows with small δ. Austin and Seader[6] solved the Navier–Stokes equations in the vorticity–stream-function form numerically for the flow within a rigorously treated toroidal geometry (i.e. no assumption on δ) and obtained solutions up to $\kappa = 1008$ for $\delta = 1/9{\cdot}06$. (Some numerical analysts dealing with developing duct flow, as well as experimental workers, find it convenient to introduce another Dean number, $\kappa = (2W_m a/\nu)\delta^{1/2}$, where W_m is the mean axial velocity.) Dennis and Ng[7] extended McConalogue and Srivastava's Fourier series analysis and obtained solutions up to $D = 5000$, which corresponds to $\kappa = 369{\cdot}5$.

For developing flow in a curved pipe, Soh and Berger[8] showed that even when the axial flow appears to be fully developed, especially near the inner bend, at relatively large downstream locations the secondary flow in the core region still oscillates in magnitude, with the flow near the

* Senior Research Engineer at Sverdrup Technology Inc., NASA Lewis Research Center, Cleveland, OH 44135, U.S.A.

0271–2091/87/070733–23$11.50

Received 1 August 1986
Revised 24 November 1986

wall gradually becoming unchanging as the flow proceeds downstream. Oscillations in the secondary flow are more conspicuous for high Dean numbers, implying that a very large value for the last downstream station in θ, at which the flow is fully developed, should be used to obtain solutions for high κ. It therefore seems to be very difficult and numerically wasteful to obtain the fully developed flow field from a developing-flow calculation.

It is the aim of this paper to solve the full Navier–Stokes equations for the fully developed flow of a homogeneous Newtonian fluid in a curved pipe of circular cross-section for *arbitrary* curvature ratio δ. Obtaining second-order accurate numerical solutions using central difference formulations without adding artificial damping terms we shall be able to determine the effect of δ on the flow.

2. MATHEMATICAL FORMULATION OF THE PROBLEM

Figure 1 shows the toroidal co-ordinate system used in the analysis. Here r' is the radial distance from the centre of the pipe O, ϕ the circumferential angle measured from the positive x' axis and θ the streamwise angular distance. The velocity components corresponding to the (r', ϕ, θ) co-ordinates are (u', v', w'). Non-dimensionalizing velocities, distances, time t' and pressure p' by W_0, a, a/W_0 and ρW_0^2, respectively, where ρ is the density and W_0 the reference velocity, defined in Section 4, we can write the Navier–Stokes equations for the fully developed flow as

$$\frac{\partial u}{\partial t} + \mathbf{S}u - \frac{v^2}{r} - \frac{\delta \cos\phi}{B} w^2 = -\frac{1}{h_1}\frac{\partial p}{\partial r} + \frac{1}{R_0}\left[\mathbf{T}u - \frac{1}{r^2}\left(2\frac{\partial v}{\partial \phi} + u\right) + \frac{\delta v \sin\phi}{rB} - \frac{\delta^2 \cos\phi}{B^2}(u\cos\phi - v\sin\phi)\right], \tag{1}$$

$$\frac{\partial v}{\partial t} + \mathbf{S}v + \frac{uv}{r} + \frac{\delta \sin\phi w^2}{B} = -\frac{1}{h_2}\frac{\partial p}{\partial \phi} + \frac{1}{R_0}\left[\mathbf{T}v + \frac{1}{r^2}\left(2\frac{\partial u}{\partial \phi} - v\right) - \frac{\delta u \sin\phi}{rB} + \frac{\delta^2 \sin\phi}{B^2}(u\cos\phi - v\sin\phi)\right], \tag{2}$$

$$\frac{\partial w}{\partial t} + \mathbf{S}w + \frac{\delta w}{B}(u\cos\phi - v\sin\phi) = \frac{1}{B} + \frac{1}{R_0}\left[\mathbf{T}w - \frac{\delta^2 w}{B^2}\right], \tag{3}$$

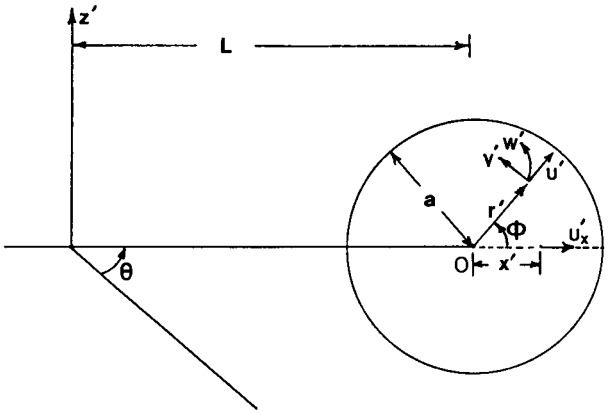

Figure 1. Toroidal co-ordinate system

$$\frac{1}{J}\left[\frac{\partial}{\partial r}(h_2 Bu)+\frac{\partial}{\partial \phi}(h_1 Bv)\right]=0, \tag{4}$$

where J is h_1h_2B, $B=1+\delta r\cos\phi, h_1=1, h_2=r$, and the operators $\mathbf{S}$ and $\mathbf{T}$ are defined by

$$\mathbf{S}=\frac{1}{J}\left[\frac{\partial}{\partial r}(h_2 Bu\,\cdot)+\frac{\partial}{\partial \phi}(h_1 Bv\,\cdot)\right]$$

and

$$\mathbf{T}=\frac{1}{J}\left[\frac{\partial}{\partial r}\left(\frac{h_2 B}{h_1}\frac{\partial\cdot}{\partial r}\right)+\frac{\partial}{\partial \phi}\left(\frac{h_1 B}{h_2}\frac{\partial\cdot}{\partial \phi}\right)\right].$$

The reference velocity and R_0 are defined as

$$W_0=\left[\frac{a}{\rho L}\left(-\frac{\partial p'}{\partial \theta}\right)\right]^{1/2}=\left(\frac{a}{\rho}G\right)^{1/2} \tag{5}$$

and

$$R_0=W_0 a/\nu, \tag{6}$$

where G, the pressure gradient, is given by $-(1/L)(\partial p'/\partial\theta)$; the Dean number D is related to the Reynolds number R_0 by

$$D=R_0^2(2\delta)^{1/2}. \tag{7}$$

The term $1/B$ appearing in (3), which approaches unity as $\delta\to 0$, is the dimensionless pressure gradient necessary to maintain the flow.

The no-slip boundary condition at the wall requires that

$$u=v=w=0 \quad \text{at} \quad r=1. \tag{8}$$

Because the flow is symmetric about the x-axis it follows that

$$v=\frac{\partial u}{\partial \phi}=\frac{\partial w}{\partial \phi}=0, \quad \text{for} \quad \phi=0,\pi. \tag{9}$$

The plane $z=0$, where each cross-sectional view coincides with the x-axis, is called the plane of symmetry.

Equations (1)–(4) with boundary conditions (8), (9) are to be integrated in time as an initial-value problem. The pressure–velocity[9] and Poisson equation methods[10] for the pressure are commonly used for that purpose. Any of these methods are computationally wasteful if our goal is to obtain a steady solution only because $\nabla\cdot\mathbf{u}=0$ has to be satisfied at every time step.

To find the steady solution of the Navier–Stokes equations Chorin[11] introduced the following auxiliary system:

$$\frac{\partial \mathbf{u}}{\partial t}+\nabla\cdot(\mathbf{uu})=-\nabla p+\frac{1}{Re}\nabla^2\mathbf{u} \tag{10}$$

and

$$\xi\frac{\partial p}{\partial t}+\nabla\cdot\mathbf{u}=0. \tag{11}$$

The constraint $\nabla\cdot\mathbf{u}=0$ is replaced by the evolution equation (11). The ξ appearing in (11) is called the coefficient of artificial compressibility and plays a role similar to that of a relaxation parameter. To apply the artificial compressibility method to our problem, the equations to be solved are (1)–(3) and the evolution form of the continuity equation,

$$\xi\frac{\partial p}{\partial t}+\frac{1}{J}\left[\frac{\partial}{\partial r}(h_2Bu)+\frac{\partial}{\partial\phi}(h_1Bv)\right]=0, \tag{12}$$

subject to boundary conditions (8), (9) and specified initial conditions on $\mathbf{u}$ and p for given parameters R_0 and δ.

3. NUMERICAL FORMULATION

The Navier–Stokes equations with artificial compressibility, (1)–(3) and (12), can be rewritten as

$$\frac{\partial\mathbf{H}}{\partial t}+(\mathbf{A}_r+\mathbf{A}_\phi)\mathbf{H}+\mathbf{C}=\mathbf{0}, \tag{13}$$

where

$$\mathbf{H}=\begin{bmatrix}u\\ v\\ w\\ p\end{bmatrix},\quad \mathbf{A}_r=\begin{bmatrix}M & 0 & 0 & \frac{1}{h_1}\frac{\partial}{\partial r}\\ 0 & M & 0 & 0\\ 0 & 0 & M & 0\\ \frac{1}{\xi J}\frac{\partial}{\partial r}(h_2B\cdot) & 0 & 0 & 0\end{bmatrix},\quad \mathbf{A}_\phi=\begin{bmatrix}N & 0 & 0 & 0\\ 0 & N & 0 & \frac{1}{h_2}\frac{\partial}{\partial\phi}\\ 0 & 0 & N & 0\\ 0 & \frac{1}{\xi J}\frac{\partial}{\partial\phi}(h_1B\cdot) & 0 & 0\end{bmatrix},$$

$$\mathbf{C}=\begin{bmatrix}-(v^2/r)-\delta\cos\phi(w^2/B)-R_0^{-1}\{-[(2\partial v/\partial\phi+u)/r^2]+(\delta v\sin\phi/rB)-\delta^2\cos\phi(u\cos\phi-v\sin\phi)/B^2\}\\ (uv/r)+\delta\sin\phi(w^2/B)-R_0^{-1}\{[(2\partial u/\partial\phi-v)/r^2]-(\delta u\sin\phi/rB)+\delta^2\sin\phi(u\cos\phi-v\sin\phi)/B^2\}\\ [\delta w(u\cos\phi-v\sin\phi)/B]-B^{-1}+(R_0^{-1}\delta^2w/B^2)\\ 0\end{bmatrix}$$

and

$$M=\frac{1}{J}\left\{\frac{\partial}{\partial r}(h_2Bu\cdot)-\frac{1}{R_0}\frac{\partial}{\partial r}\left(\frac{h_2B}{h_1}\frac{\partial\cdot}{\partial r}\right)\right\},$$

$$N=\frac{1}{J}\left\{\frac{\partial}{\partial\phi}(h_1Bv\cdot)-\frac{1}{R_0}\frac{\partial}{\partial\phi}\left(\frac{h_1B}{h_2}\frac{\partial\cdot}{\partial\phi}\right)\right\}.$$

Introducing an intermediate step, denoted by *, and approximating the convection terms with the values at time $n\Delta t$, we can advance (13) in time using the algorithm

$$\left.\begin{aligned}\mathbf{H}^*-\mathbf{H}^n+\Delta t(\mathbf{A}_r^n\mathbf{H}^n+\mathbf{A}_\phi^n\mathbf{H}^*+\mathbf{C}^n)=0\\ \mathbf{H}^{n+1}-\mathbf{H}^n+\Delta t(\mathbf{A}_r^n\mathbf{H}^{n+1}+\mathbf{A}_\phi^n\mathbf{H}^*+\mathbf{C}^n)=0\end{aligned}\right\}. \tag{14}$$

These equations can be written in a simpler 'delta form' as

$$(\mathbf{I}+\Delta t\,\mathbf{A}_\phi^n)\Delta\mathbf{H}^*=-\Delta t(\mathbf{A}_\phi^n+\mathbf{A}_r^n)\mathbf{H}^n-\Delta t\,\mathbf{C}^n \tag{15}$$

$$(\mathbf{I}+\Delta t\,\mathbf{A}_r^n)\Delta\mathbf{H}^{n+1}=\Delta\mathbf{H}^* \tag{16}$$

where $\Delta\mathbf{H}^*=\mathbf{H}^*-\mathbf{H}^n$, $\Delta\mathbf{H}^{n+1}=\mathbf{H}^{n+1}-\mathbf{H}^n$ and $\mathbf{I}$ is the identity matrix.

The numerical scheme above will be employed in a strict central-difference form for the staggered grid system shown in Figure 2. We call the calculation procedure for (15) the ϕ-sweep, that for (16)

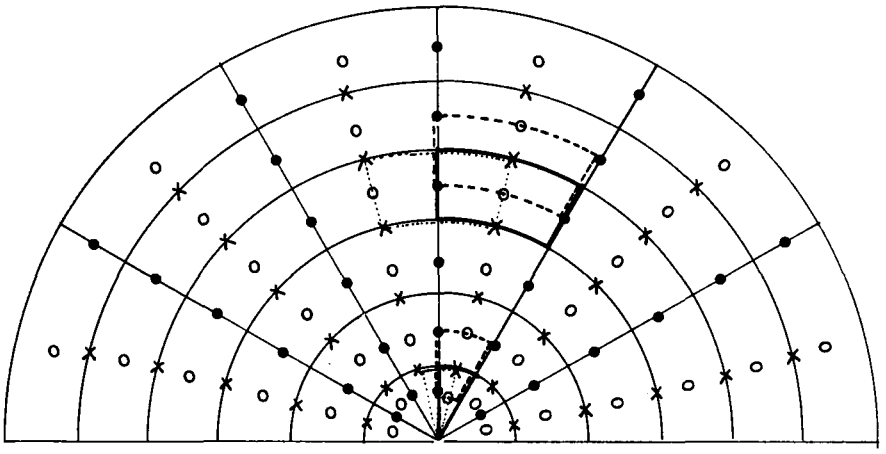

Figure 2. Schematic arrangement of the staggered grid; ○ pressure and w; × u-velocity; ● v-velocity; and ——pressure or w-cell; ---- u-cell; .... v-cell

the r-sweep. During the ϕ-sweep Δv^* and Δp^* are coupled to yield a 2×2 block tridiagonal matrix, whereas Δu^* is decoupled from the pressure. During the r-sweep Δu^{n+1} and Δp^{n+1} are coupled, with Δv^{n+1} decoupled from the pressure. The central-difference formulation in the staggered grid has the property that pressure is two-point central-differenced in each sweep. The velocity–pressure coupling and two-point central-differencing of the pressure make the system (15), (16) stable without introducing artificial damping terms. Details of the central-difference formulations are given in the Appendix.

Owing to the presence of a boundary layer for large R_0, in which velocity changes rapidly for both the main and secondary flows, a co-ordinate stretching is advisable near the wall, such that fine grid lines are clustered near $r = 1$ and equidistance is maintained in the computational domain. To do this we introduce an r-co-ordinate stretching function

$$r = f(\eta) = \frac{\ln(s\eta/\mathrm{II} + 1)}{\ln(s + 1)} \tag{17}$$

where II is the number of grid points in the r-direction, and s is the value representing the degree of stretching. Then, h_1 becomes $f'(\eta)$ and Δr is $f'(\eta)$, fixing $\Delta\eta = 1$. The $\partial/\partial r$ in the Navier–Stokes equations is then simply replaced by $\partial/\partial\eta$.

The treatment of the centre, r or $\eta = 0$, requires some care. In particular, the calculation of momentum flux and $\partial u/\partial\eta$ on the η^--face of the first ith u-cell in the η direction using the present staggered grid calls for the value of u at the centre. The exact values of u and v can be written for the flow symmetric with respect to $z = 0$ as

$$u = u_0 \cos\phi \quad \text{and} \quad v = -u_0 \sin\phi, \tag{18}$$

where u_0 is the x-component of velocity at $\eta = 0$. The best numerical approximation to u_0 is

$$u_0 = (u_{1,1} - u_{1,JJ})/2, \tag{19}$$

where JJ is the number of grid spacings in the ϕ-direction. Since only the asymptotic steady-state solution is of interest, we can choose a spatially varying time step to accelerate convergence, allowing Δt to vary in space for a fixed Courant number, C_r, according to

$$\Delta t_{i,j} = \frac{C_r}{\frac{1}{2}\left(\frac{|u|}{h_1} + \frac{|v|}{h_2 \Delta\phi}\right) + \left[\frac{1}{4}\left(\frac{|u|}{h_1} + \frac{|v|}{h_2\Delta\phi}\right)^2 + \frac{2}{\xi}\left(\frac{1}{h_1^2} + \frac{1}{h_2^2 \Delta\phi^2}\right)\right]^{1/2}}. \tag{20}$$

The details of choosing C_r and ξ are described in Reference 12.

4. RESULTS AND DISCUSSION

Calculations were performed for the range $5 \leqslant D \leqslant 30{,}000$ for three values of δ: 0·01, 0·1 and 0·2. A strict central difference scheme with a 25×40 grid was used throughout inside the computational domain. A steady-state is considered reached if the local maximum of the divergence of velocity, $\max(\nabla \cdot \mathbf{u})_{i,j}$, is less than $10^{-5} \sim 5 \times 10^{-5}$; the coefficient of artificial compressibility, ξ, is taken to lie between 1 and 3×10^{-2} depending upon the values of D and δ. The Courant number, C_r, is taken as $15 \sim 30$. The numbers of time steps to reach steady-state are $120 \sim 700$ according to the values of D and δ.

For s, the stretching parameter described in (17), two values, 1 and 10, have been used for D less than and greater than 14,000, respectively. We call the cases $s = 1$ and 10 cases (I) and (II), respectively. Figure 3(a), exhibiting the pressure or the axial velocity grids, shows the axial velocity profiles along the x-axis, whereas Figure 3(b) shows the locations of the u-velocities and the u_x velocity profile. Agreement of the w and u_x-velocity profiles for cases (I) and (II) is excellent, suggesting that the numerical scheme used in the present study is almost grid-size independent.

Before a physical interpretation can be given to the results it is necessary to determine the relationship between the dimensionless parameter R_0 and the Reynolds number based upon the mean axial velocity W_m. This velocity is given by

$$W_m = \frac{2}{\pi a^2}\int_0^a \int_0^\pi W_0 w r' \, dr' \, d\phi = \frac{2W_0}{\pi}\int_0^1 \int_0^\pi w r \, dr \, d\phi. \tag{21a}$$

Therefore, $W_m = (2I/\pi)W_0$, where

$$I = \int_0^1 \int_0^\pi w r \, dr \, d\phi, \tag{21b}$$

and the Reynolds number, Re, becomes

$$Re = W_m a/\nu = (W_0 a/\nu)\frac{2I}{\pi} = R_0 \frac{2I}{\pi}. \tag{22}$$

Clearly, the mean axial velocity, and hence Re, can be determined only after each calculation is completed. Basing the Dean number κ upon W_m, i.e. $\kappa = (2W_m a/\nu)\delta^{1/2}$, is in many ways more convenient and useful to experimental workers and those treating developing flow.

The friction ratio f_c/f_s, defined as the ratio of the pressure gradient in a curved pipe to that in a straight pipe for the same flow rate, is given by the expression

$$\frac{f_c}{f_s} = \frac{Q_s}{Q_c} = \frac{\frac{\pi G a^4}{8\mu}}{\int_0^a \int_0^\pi W_0 w r' \, dr' \, d\phi} = \frac{\pi G a^4}{16\pi a^2 \mu W_0 I} = \frac{\pi R_0}{16 I}, \tag{23}$$

where Q_c/Q_s is the ratio of the flow rate in a curved pipe to that in a straight pipe for the same

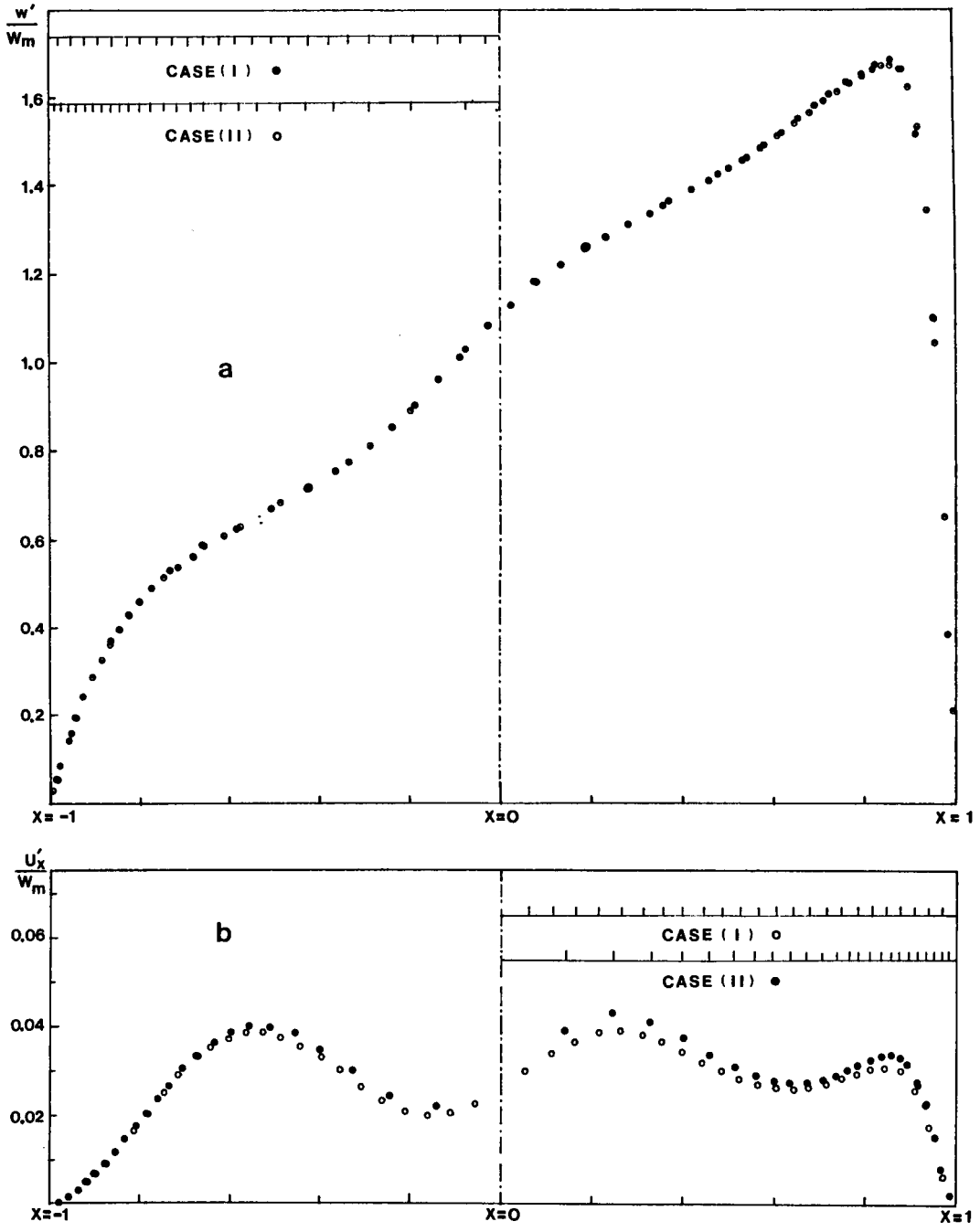

Figure 3. (a) Grid effects on the w'/W_m—profile for $\delta = 0{\cdot}01$ and $D = 20{,}000$. (b) Grid effects on the u'_x/W_m—profile for $\delta = 0{\cdot}2$ and $D = 24{,}000$

pressure gradient. Table I contains the calculated values of Re, κ and f_c/f_s for the different values of D and δ. Comparisons of the results obtained from using different values of s are made in

Table I. Dean numbers (D and κ), Reynolds numbers and friction ratios

D	$1/\delta$	Re	κ	f_c/f_s
5	5	0·9902	0·8857	0·9980
	10	1·3996	0·8852	0·9985
	100	4·4253	0·8851	0·9987
10	5	1·9798	1·7708	0·9983
	10	2·7988	1·7701	0·9987
	100	8·8504	1·7701	0·9987
96	5	18·1369	16·2221	1·0461
	10	25·9351	16·4028	1·0346
	100	82·9387	16·5877	1·0231
200	5	33·9172	30·3365	1·1654
	10	48·7748	30·8479	1·1461
	100	156·9089	31·3818	1·1266
500	5	71·0435	63·5432	1·3910
	10	102·4867	64·8182	1·3636
	100	330·7375	66·1475	1·3362
1,000	5	122·5533	109·6150	1·6127
	10	176·8413	111·8442	1·5806
	100	570·7082	114·1416	1·5488
2,000	5	205·2341	183·5669	1·9260
	10	296·3301	187·4156	1·8865
	100	956·8378	191·3675	1·8475
5,000	5	398·6581	356·5706	2·4789
	10	575·5788	364·0279	2·4281
	100	1858·681	371·7362	2·3777
7,000	5	508·2507	454·5932	2·7221
	10	733·5694	463·9500	2·6672
	100	2368·287	473·6574	2·6125
10,000	5	656·2792	586·9939	3·0116
	10	947·3339	599·1465	2·9505
	100	3057·538	611·5075	2·8908
14,000	5	837·8993	749·4399	3·3023
	10	1209·316	764·8382	3·2358
	100	3899·487	779·8972	3·1733
16,000	5	920·1880	823·0412	3·4366
18,000	5	998·9766	893·5118	3·5612
	10	1440·440	911·0142	3·4928
	100	4646·050	929·2099	3·4244
20,000	5	1074·665	961·2092	3·6782
	10	1549·312	979·8708	3·6082
	100	4999·287	999·8570	3·5360
24,000	5	1217·795	1089·229	3·8951
	10	1756·626	1110·988	3·8188
	100	5666·220	1133·244	3·7438
26,000	5	1285·664	1149·933	3·9969
	10	1854·457	1172·861	3·9188
30,000	5	1417·563	1267·907	4·1827
	10	2044·461	1293·031	4·1015

Table II. Variation of numerical results with grid

		Case (I)			Case (II)		
D	$1/\delta$	Re	κ	f_c/f_s	Re	κ	f_c/f_s
14,000	5	832·4593	744·5742	3·3239	837·8993	749·4399	3·3023
	100	3879·104	775·8207	3·1900	3899·487	779·8972	3·1733
18,000	5	991·5052	886·8292	3·5880	998·9766	893·5118	3·5612
	100	4620·595	924·1189	3·4433	4646·050	929·2099	3·4244
20,000	5	1065·927	953·3937	3·7084	1074·665	961·2092	3·6782
	100	4961·693	992·3385	3·5628	4999·287	999·8570	3·5360
24,000	5	1207·462	1079·987	3·9284	1217·5951	1089·229	3·8951
	100	5617·777	1123·555	3·7761	5666·220	1133·244	3·7438

Table II, and show that all of the results for each D and δ differ by less than 1 per cent from each other, further supporting the grid independence of the present numerical scheme. The present values of κ and f_c/f_s for $\delta = 0{\cdot}01$ agree excellently with those of Dennis,[13] who obtained solutions for the range $96 \leqslant D \leqslant 5000$. Even at the highest values of D we were unable, despite our most vigorous efforts, to find a four-vortex family of solutions.[7,14]

Curvature effect on the friction ratio

The friction ratio, f_c/f_s, plotted against $\kappa^{1/2}$ is illustrated in Figure 4 for the three values of δ. This is drawn in such a way that two neighbouring data points are connected by a straight line. Except for a low Dean number region (κ less than about 16), f_c/f_s varies almost linearly with $\kappa^{1/2}$ and tends to have higher values as δ increases for the same κ. The variation of f_c/f_s with δ may be best described if we have the values of f_c/f_s for the exactly same κ. Unfortunately this is almost impossible, because κ is only obtained as a part of the solution for a fully developed flow; therefore, to observe the behaviour of f_c/f_s with δ, the friction ratio for $\delta = 0{\cdot}2$ is interpolated with a linear function of $\kappa^{1/2}$ between two neighbouring data points to yield the value of f_c/f_s for the same κ of the case $\delta = 0{\cdot}01$. We define the following to examine the curvature effect:

$$d(\kappa) = \frac{\left[\frac{f_c}{f_s}(\kappa)\right]_{\delta=0{\cdot}2} - \left[\frac{f_c}{f_s}(\kappa)\right]_{\delta=0{\cdot}01}}{\left[\frac{f_c}{f_s}(\kappa)\right]_{\delta=0{\cdot}01}} \tag{24}$$

where $(f_c/f_s)_{\delta=0{\cdot}01}$ is the friction ratio at $\delta = 0{\cdot}01$, $[f_c/f_s]_{\delta=0{\cdot}2}$ the interpolated one at $\delta = 0{\cdot}2$ for the same κ as at $\delta = 0{\cdot}01$. The $d(\kappa)$ can be considered as a measure for examining the effect of curvature. As shown in Table III, $d(\kappa)$ increases as κ becomes larger; therefore the curvature effect on f_c/f_s must not be underestimated for high κ.

For very low κ, the curvature effect on f_c/f_s is quite reversed; that is, for κ less than about 2 (see Table I), the friction ratio itself is less than unity and, moreover, f_c/f_s gets smaller as δ increases. These surprising phenomena have been reported in the series expansion studies by Topakoglu[15] and Larrain and Bonilla.[16]

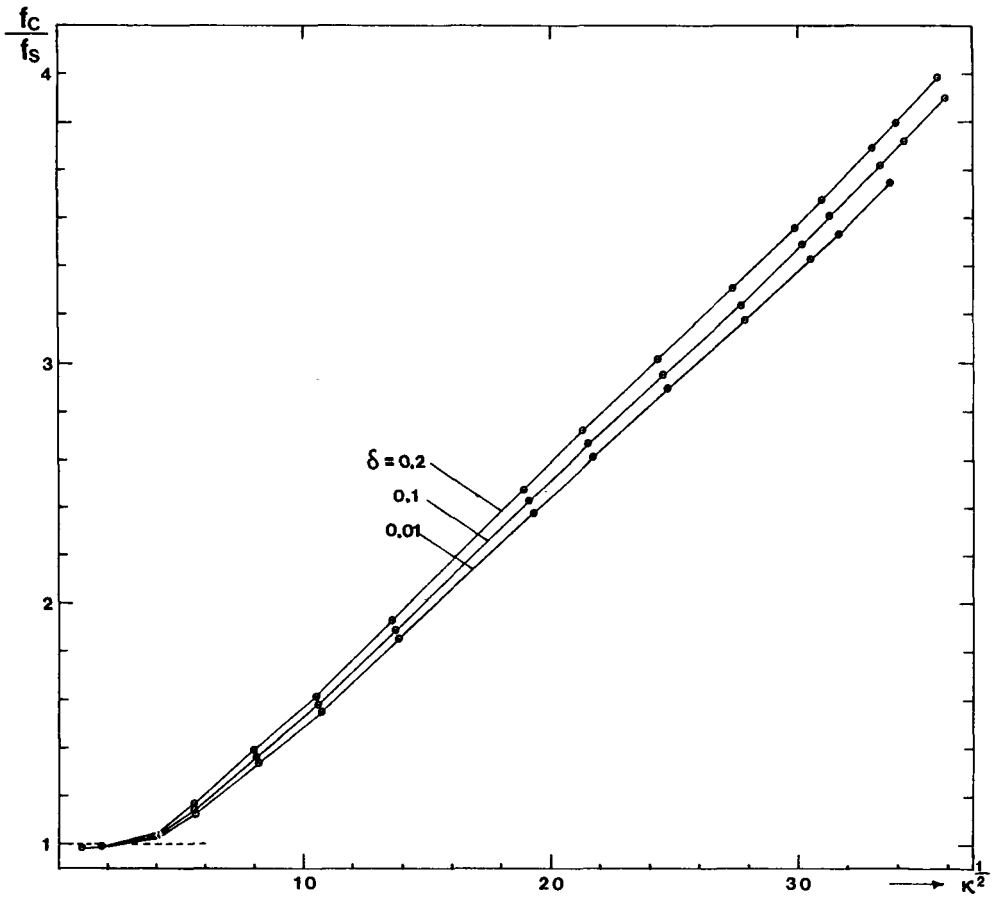

Figure 4. Friction ratio vs. $\kappa^{1/2}$

Table III. Effect of curvature on the friction ratio

κ	$1/\delta$	f_c/f_s	$d(\kappa)$ in %
0·885	5	0·9980	−0·07
	100	0·9987	
1·770	5	0·9983	−0·04
	100	0·9987	
16·588	5	1·0497	2·60
	100	1·0231	
66·148	5	1·4054	5·18
	100	1·3362	
114·142	5	1·6345	5·53
	100	1·5488	
611·508	5	3·0578	5·78
	100	2·8908	
779·897	5	3·3587	5·84
	100	3·1733	
1133·244	5	3·9692	6·02
	100	3·7438	

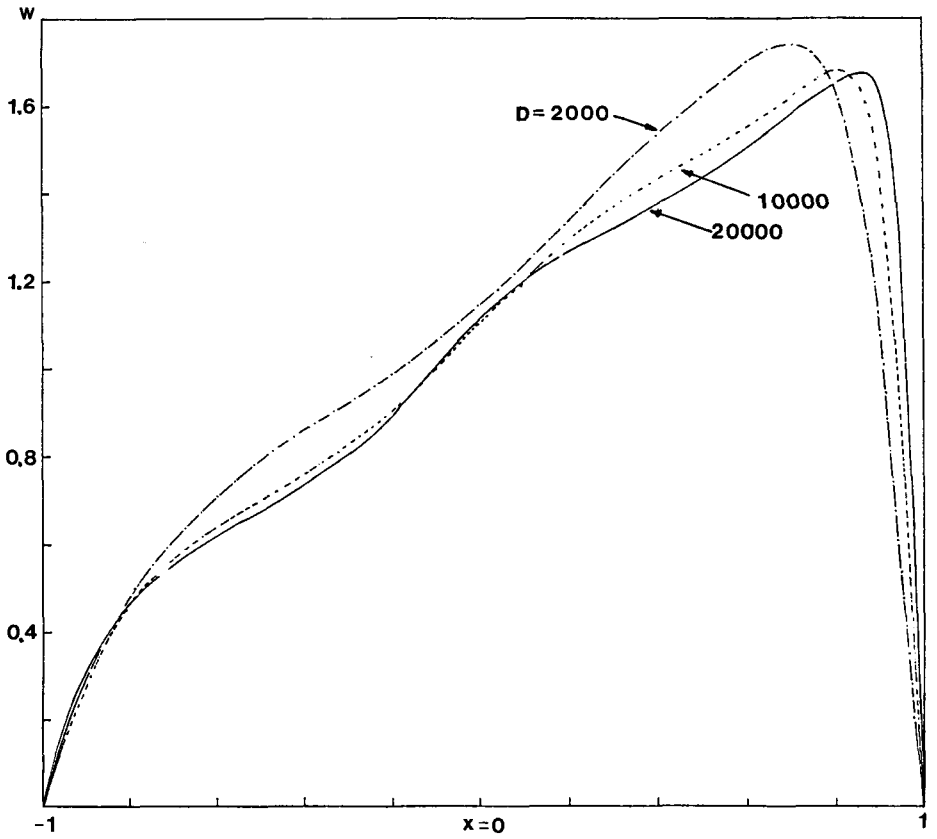

Figure 5(a). w-profile on the plane of symmetry for $\delta = 0{\cdot}01$

Main flow

For future discussion let us redefine the dimensionless velocities u, v, w and u_x to be non-dimensionalized by the mean velocity W_m, that is $u = u'/W_m$, etc. Figures 5(a), (b) and (c) show axial velocity profiles along the plane of symmetry for $\delta = 0{\cdot}01$, $0{\cdot}1$ and $0{\cdot}2$, and $2000 \leqslant D \leqslant 30{,}000$. We see that for a given δ the maximum value of w decreases and its location shifts further toward the outer bend ($x = 1$) as D or κ increases. For $\delta = 0{\cdot}01$ and $\kappa = 191{\cdot}37$, $611{\cdot}51$ and $999{\cdot}86$ the maximum value of w is $1{\cdot}74$ at $x = 0{\cdot}71$, $1{\cdot}68$ at $x = 0{\cdot}81$ and $1{\cdot}67$ at $x = 0{\cdot}87$, respectively. For $\delta = 0{\cdot}1$ and $\kappa = 187{\cdot}42$, $599{\cdot}15$ and $1293{\cdot}03$ the maximum values of w are $1{\cdot}67$ at $x = 0{\cdot}68$, $1{\cdot}61$ at $x = 0{\cdot}80$ and $1{\cdot}59$ at $x = 0{\cdot}89$, respectively. And, finally for $\delta = 0{\cdot}2$ and $\kappa = 183{\cdot}57$, $586{\cdot}99$ and $1267{\cdot}91$, w has maximum values of $1{\cdot}61$ at $x = 0{\cdot}67$, $1{\cdot}53$ at $x = 0{\cdot}79$ and $1{\cdot}51$ at $x = 0{\cdot}88$, respectively. For the same D, assuming that κ falls in the same range, the maximum value of w decreases as δ increases, which indicates that the axial velocity is more evenly distributed for larger δ because of the stronger secondary flow. This is apparent in Figure 6 where the axial velocity contours of the high velocity regime for $\delta = 0{\cdot}2$ are seen to occupy a larger area than those for $\delta = 0{\cdot}01$.

Figures 5(a), (b) and (c) also illustrate that as κ increases the axial velocity profiles become more distorted and have more inflexion points; for example, for $\delta = 0{\cdot}1$, a single inflexion point is present for $\kappa = 187{\cdot}42$, and two inflexion points for $\kappa = 599{\cdot}15$, and these become more

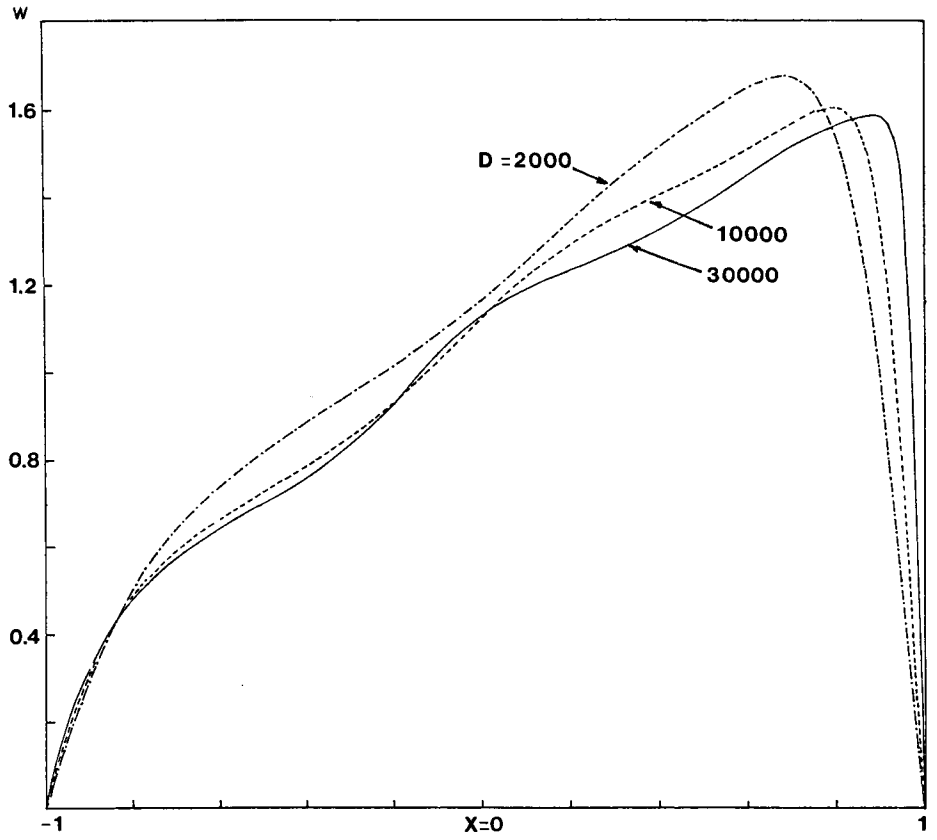

Figure 5(b). w-profile on the plane of symmetry for $\delta = 0{\cdot}1$

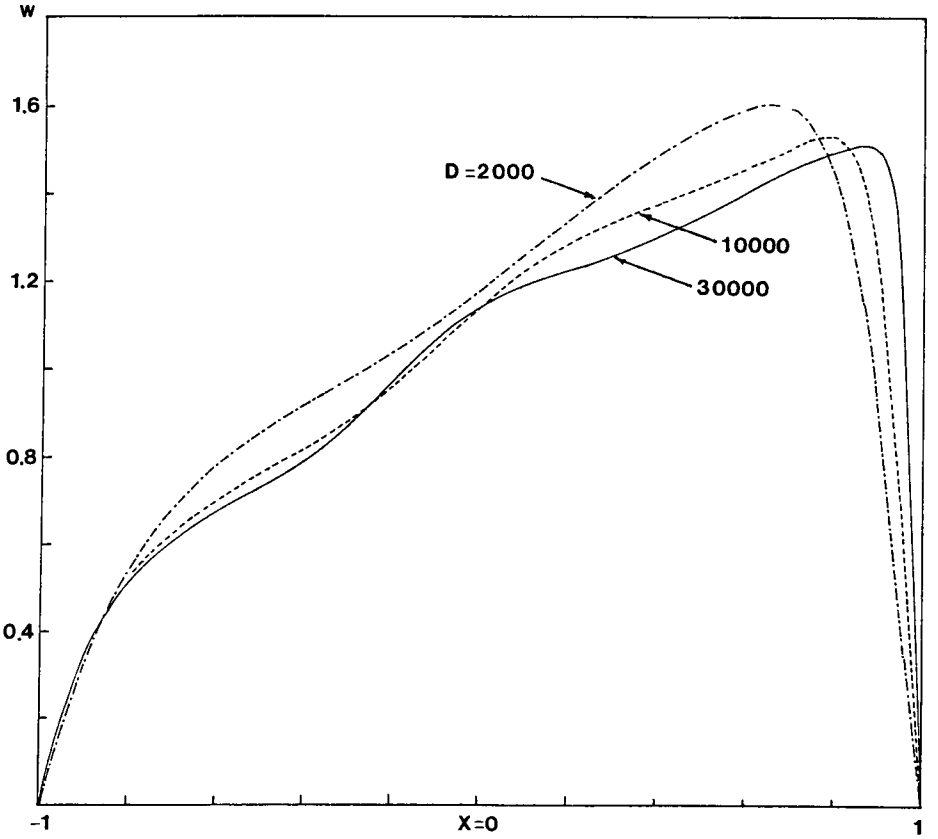

Figure 5(c). w-profile on the plane of symmetry for $\delta = 0{\cdot}2$

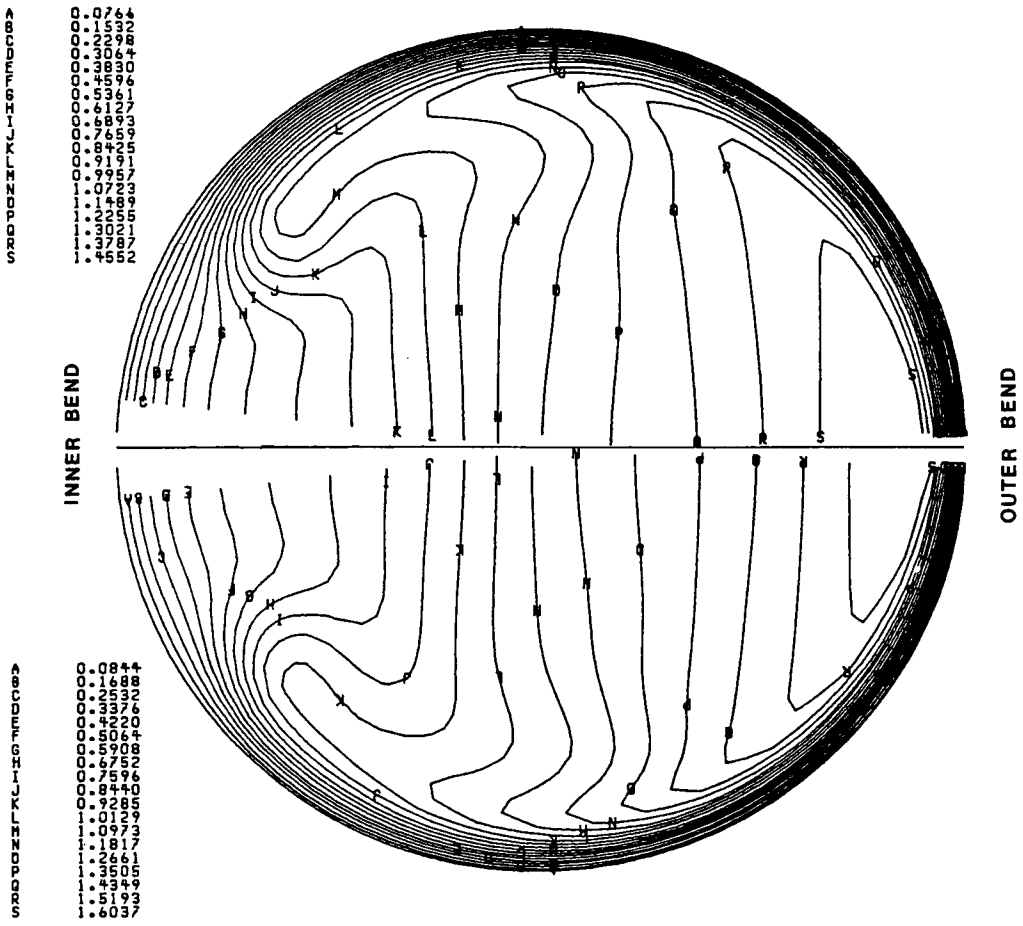

Figure 6. Axial velocity, w, contour: upper half—$\delta = 0{\cdot}2$ and $D = 24{,}000$ ($\kappa = 1089{\cdot}23$); lower half—$\delta = 0{\cdot}01$ and $D = 24{,}000$ ($\kappa = 1133{\cdot}24$)

conspicuous as κ increases, leading to velocity profiles as complicated as that shown for $\kappa = 1293{\cdot}03$. Velocity profiles containing multiple inflexion points have been reported experimentally by Agrawal *et al.*[17] (see their Figure 5(e), the curve denoted by Δ). In Figure 6 we also see that for high κ there exists a region where the isovelocity lines double back on themselves; thus a local second maximum appears if the axial velocity profile is plotted along a plane parallel to the plane of symmetry. This does not occur for low κ (see Figure 8, Reference 8). All of the above mentioned features of the axial flow can be explained in connection with the behaviour of the secondary flow, and this will be done below.

Secondary flow

A stream function for the secondary flow, ψ, is defined by

$$u = \frac{1}{rB}\frac{\partial}{\partial \phi}(B\psi), \quad v = -\frac{1}{B}\frac{\partial}{\partial r}(B\psi). \tag{25}$$

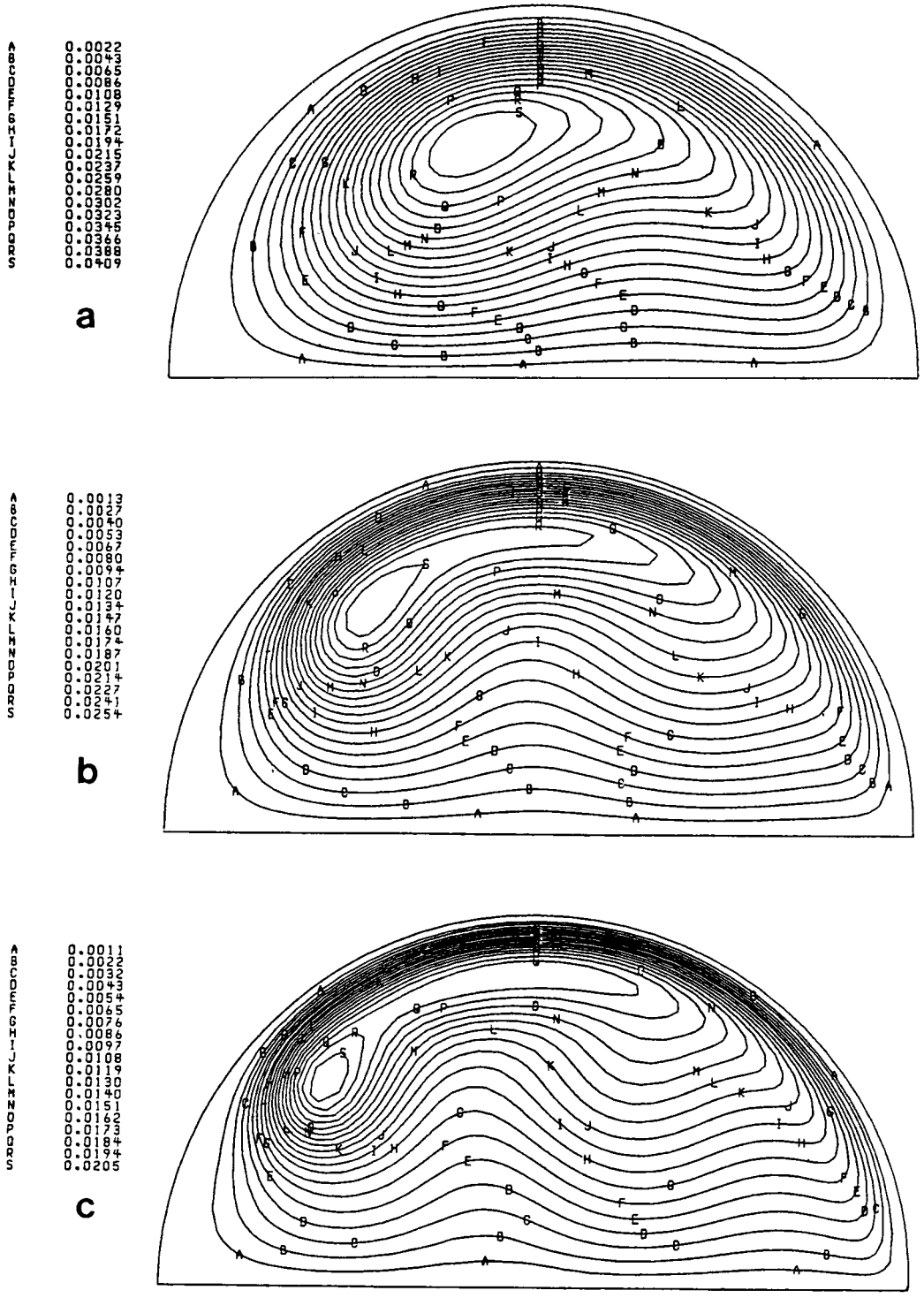

Figure 7. Streamlines for $\delta = 0{\cdot}1$: (a) $D = 2000$ ($\kappa = 187{\cdot}42$); (b) $D = 10{,}000$ ($\kappa = 599{\cdot}15$); (c) $D = 24{,}000$ ($\kappa = 1110{\cdot}99$)

Figures 7(a), (b) and (c) show the secondary flow streamlines for $\delta = 0{\cdot}1$ and various Dean numbers. The streamlines becomes more and more distorted and the location of the centre of the vortex shifts increasingly towards the inner side of the bend as κ increases. In Figures 7(b) and (c) the secondary flow streamlines are not only severely distorted, they are also elongated, so that faster moving fluid particles (i.e. larger w) near the outer bend are readily conveyed into the inner bend; this may be the reason for the appearance, for large κ, of the second maximum in the axial velocity profile in the plane parallel to the plane of symmetry.

Figures 8(a), (b) and (c) show u_x, which is u on $\phi = 0$ and $-u$ on $\phi = \pi$. For small κ a single peak occurs in the u_x profile (see Figure 19, Reference 18); this single peaked profile becomes a double-peaked and then a triple-peaked profile as κ increases. For example, for $\delta = 0{\cdot}2$, the maxima in u_x appear at $x = -0{\cdot}34$ and $0{\cdot}63$ for $\kappa = 183{\cdot}57$, and $x = -0{\cdot}53$, $0{\cdot}22$ and $0{\cdot}88$ for $\kappa = 1267{\cdot}91$. If we

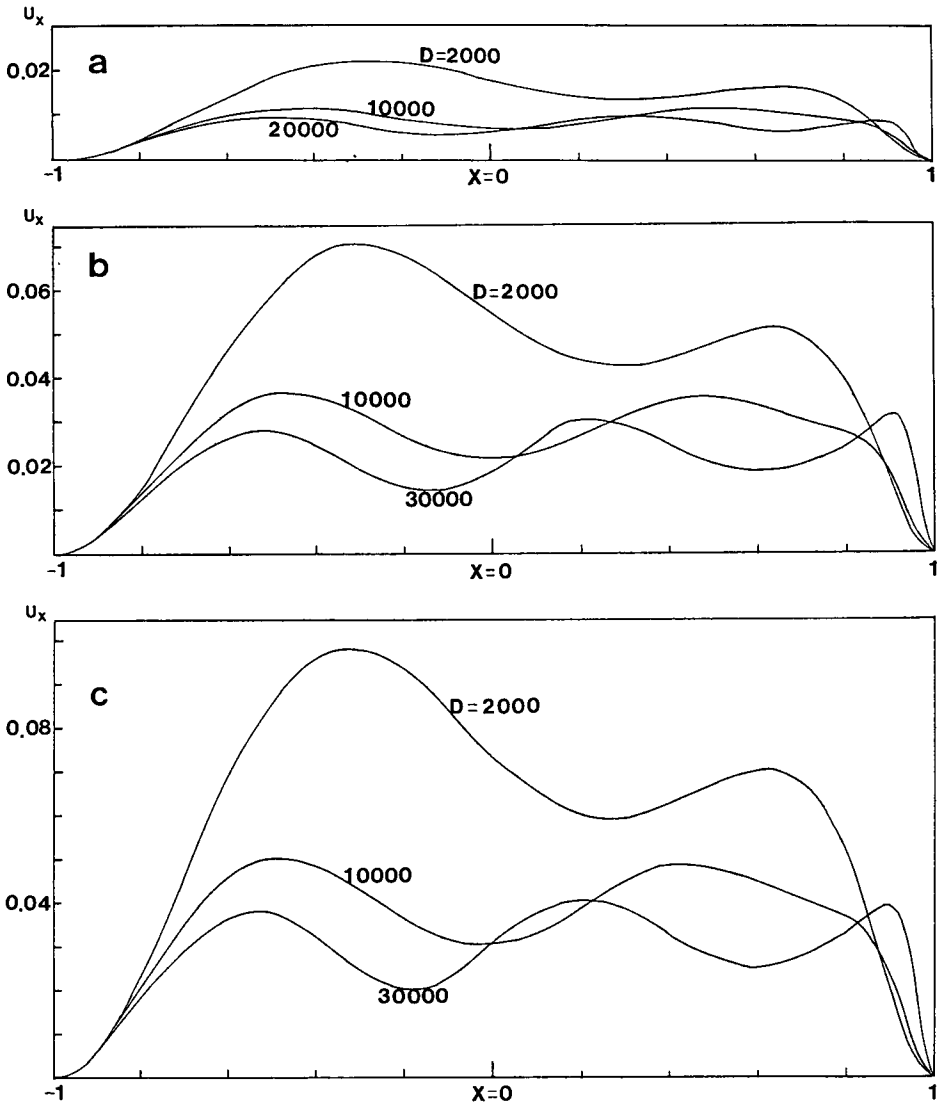

Figure 8. The u_x-profiles along the plane of symmetry for: (a) $\delta = 0{\cdot}01$; (b) $\delta = 0{\cdot}1$; (c) $\delta = 0{\cdot}2$

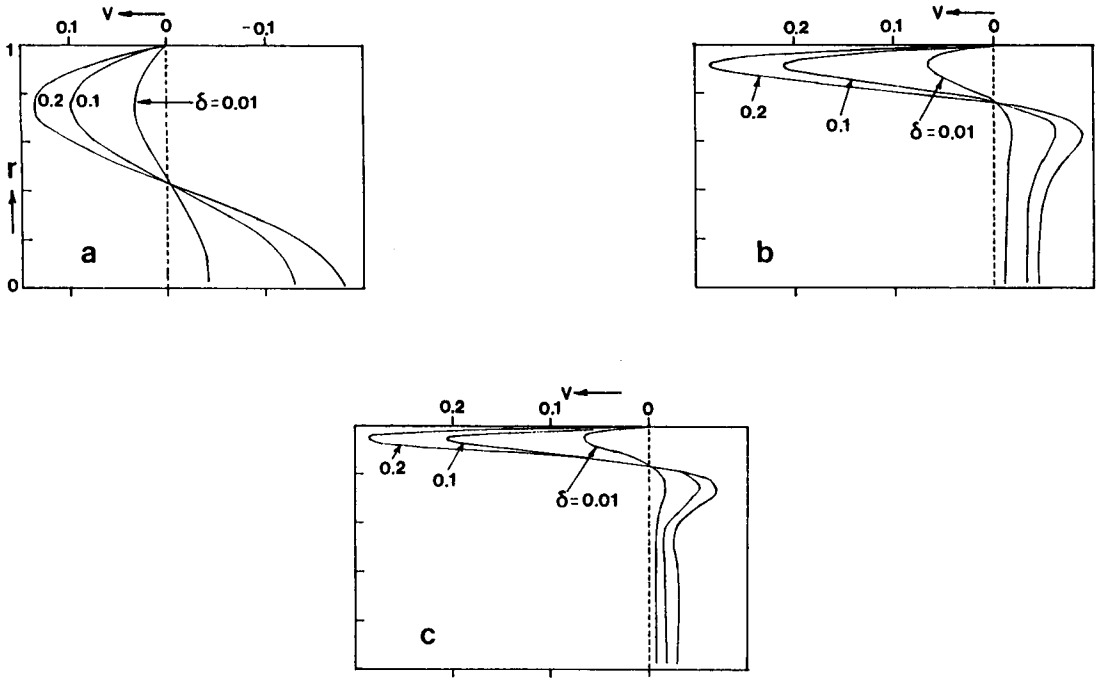

Figure 9. The v-profile at $\phi = 90°$ for (a) $D = 96$; (b) $D = 5000$; (c) $D = 20{,}000$

examine the axial velocity profiles for these κ and δ (see Figure 5(c)) it can be conjectured that $x = -0{\cdot}34$ and $0{\cdot}63$ are the inflexion and (nearly) maximum velocity points, respectively, in the w-profile for $\kappa = 183{\cdot}57$. For $\kappa = 1267{\cdot}91$, $x = -0{\cdot}53$, $0{\cdot}22$ and $0{\cdot}88$ correspond to the first and second inflexion points from the inner bend, and the maximum velocity location in the w-profile, respectively. Similar conjectures can be made for the flows for which $\delta = 0{\cdot}1$ and $0{\cdot}01$. It is also observed from Figures 8(a), (b) and (c) that the overall magnitude of u_x gets larger as δ takes on larger values.

Figures 9(a), (b) and (c) show the v-profiles at $\phi = 90°$ for $D = 96$, 5000 and 20,000, with κ having approximately the same value for each D. For $D = 96$ ($\kappa \cong 16$), the v-velocities are distributed smoothly from the centre to the wall, but it should be noted that even for the case of small κ the curvature effect is already conspicuous if one compares the maximum of $0{\cdot}03$ for $\delta = 0{\cdot}01$ with that of $0{\cdot}135$ for $\delta = 0{\cdot}2$. As D or κ increases the variation of v takes on a boundary-layer-type character, changing rapidly near the wall, as shown in Figures 9(b) and (c). For $D = 20{,}000$ ($\kappa \cong 960 \sim 1000$) the maximum of v is $0{\cdot}07$ for $\delta = 0{\cdot}01$ and $0{\cdot}29$ for $\delta = 0{\cdot}2$, which means that the order of magnitude of the relative difference in the peak velocities between $\delta = 0{\cdot}2$ and $0{\cdot}01$ remains almost the same for a wide range of D or κ (the very low κ case is excluded). From the facts that the absolute peak value increases and the boundary layer gets thinner, keeping the order of magnitude of the relative difference (about a factor of 4 between $\delta = 0{\cdot}2$ and $0{\cdot}01$ for the wide range of κ considered here) in the peak velocities the same, it is obvious that the circumferential shear stress becomes larger as δ increases for the given D or κ.

The shear stresses at the wall ($r = 1$) are defined as

$$\tau_{r\phi} = \left(\frac{\partial v}{\partial r}\right)_{r=1}, \quad \tau_{r\theta} = \left(\frac{\partial w}{\partial r}\right)_{r=1} \quad \text{and} \quad \tau_t = (\tau_{r\phi}^2 + \tau_{r\theta}^2)_{r=1}^{1/2}, \tag{26}$$

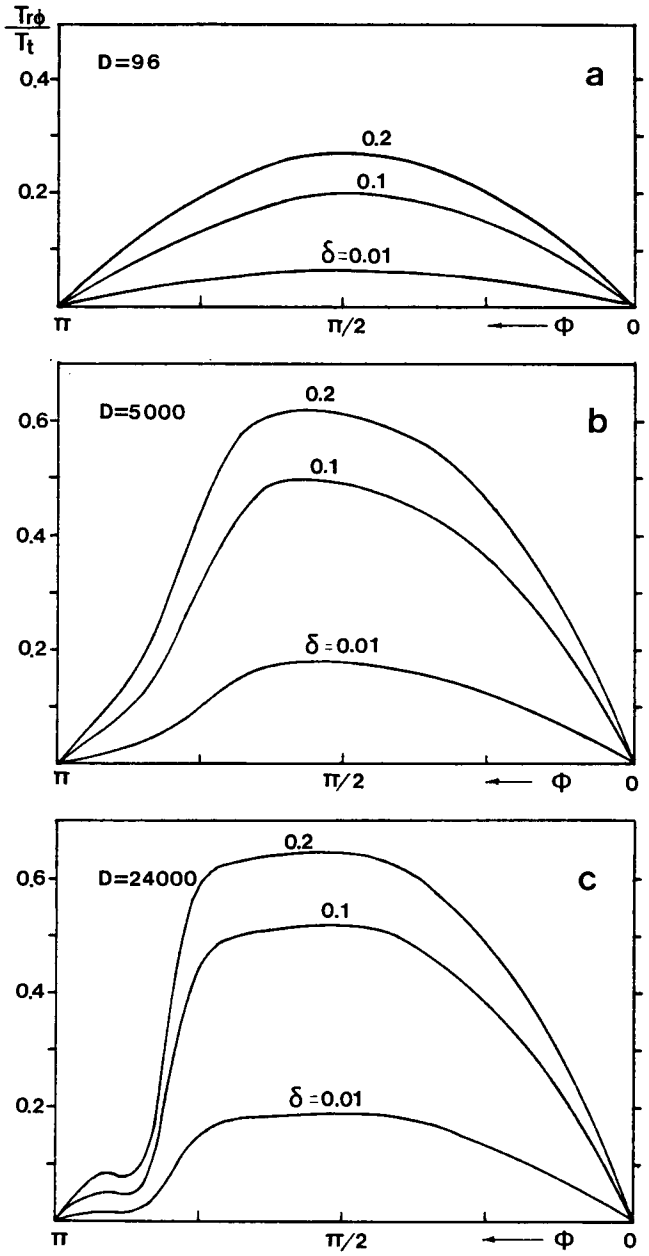

Figure 10. The fraction of circumferential shear, $\tau_{r\phi}/\tau_t$, along the torus of the wall: (a) $D = 96$; (b) $D = 5000$; (c) $D = 24{,}000$

where $\tau_{r\phi}$ is the circumferential, $\tau_{r\theta}$ the axial and τ_t the total wall shear, respectively. Figures 10(a), (b) and (c) show the variation of $\tau_{r\phi}/\tau_t$ along the wall. For $D = 96$, $\tau_{r\phi}/\tau_t$ rises as high as 0·27 and 0·20 for $\delta = 0{\cdot}2$ and 0·1, respectively, whereas it remains at a much lower 0·065 for $\delta = 0{\cdot}01$. As D or κ increases $\tau_{r\phi}/\tau_t$ becomes larger, reaching values as high as 0·65 for $\delta = 0{\cdot}2$, but remains small, less than 0·20, for $\delta = 0{\cdot}01$ (see Figure 10(c)). At $D = 96$ the difference in the peak values of $\tau_{r\phi}/\tau_t$ between $\delta = 0{\cdot}2$ and 0·01 is

about 0·2, at $D = 5000$, 0·44, and at 24,000, 0·46. These results clearly indicate that the effects of curvature on the secondary flow become greater as κ increases, and that even for low values of κ curvature effects should not be underestimated in considerations of the behaviour of the secondary flow.

As we can see in Figure 10(c) for $D = 24{,}000$ ($\kappa \cong 1090 \sim 1130$) there is a region near the inner bend where $\tau_{r\phi}/\tau_t$ drops abruptly, which becomes more striking as δ becomes larger. If we consider a boundary-layer approximation for the secondary flow marching from $\phi = 0$ toward π along the torus of the wall, then $\phi = 0$ mimics a stagnation leading edge in the development of the boundary-layer flow. As the boundary-layer type secondary flow marches toward the inner part of the bend (i.e. toward $\phi = \pi$), $\tau_{r\phi}/\tau_t$ increases gradually and then remains unchanged over a considerable distance (from Figure 10(c)), $0° < \phi < 75°$ for the increasing region, and $75° < \phi < 130°$ for the plateau region. The boundary-layer thickness remains relatively thin in this overall region $0° < \phi < 130°$, and the boundary-layer approximation is valid up to this point; beyond $\phi = 130°$ there is a precipitous drop in $\tau_{r\phi}/\tau_t$, indicating a sudden growth of the boundary-layer thickness, and the boundary-layer approximation is probably no longer appplicable. (see Reference 19, Table I, and the sudden growth in the boundary-layer thickness beginning at $-60°$.) This behaviour may explain why most boundary-layer approximations fail near the inner wall.

We can define a dimensionless shear stress as τ = total shear stress/shear stress in a straight pipe for the same Re, or

$$\tau = \frac{1}{4}\left[\left(\frac{\partial w}{\partial r}\right)^2 + \left(\frac{\partial v}{\partial r}\right)^2\right]_{r=1}^{1/2}. \tag{27}$$

Figures 11(a), (b) and (c) show τ for $500 \leqslant D \leqslant 20{,}000$ and $\delta = 0{\cdot}01$, 0·1 and 0·2, respectively. For large D, say $D = 20{,}000$, these Figures indicate precipitous drops in the total shear, which is attributable to the behaviour of the secondary flow (i.e. $\partial v/\partial r$ at $r = 1$) near the inner wall. For small δ, say $\delta = 0{\cdot}01$ or 0·1, the maximum of the total shear occurs at $\phi = 0$, but for large δ the maximum point is shifted away from $\phi = 0$, making a valley in the shear distribution for high D (see Figure 11(c) for $D = 20{,}000$). The valley becomes deeper as D or κ increase, which can be seen by the broken line in (c) for $D = 30{,}000$.

5. CONCLUSIONS

The numerical results show that the present central-differenced, factored ADI method is stable on the staggered grid, free of spurious spatial oscillations in the flow variables. We also conclude from the results that the numerical scheme is not subject to limitations on the cell Reynolds numbers, $R_0 u\Delta r$ and $R_0 vr\Delta\phi$ (u, v are non-dimensionalized with W_0), owing to the close coupling between velocity and pressure on the staggered grid. The cell Reynolds numbers appearing in the large D calculations are much larger than 2.

The artificial compressibility ξ is chosen to be the order of $1/(u^2 + v^2)$. Although we can use relatively large Courant numbers, too large a value of C_r is not recommended, because the system (15) and (16) becomes highly inconsistent with (13) for very large C_r.

As shown in Table III and Figure 4 the δ-dependency of the friction ratio increases as the Dean number increases. For high D or κ flows there appear inflection points in the w'/W_m profiles and multiple maxima in the u_x profiles. The most striking features of the δ-dependency on the flow are (i) the magnitude of the peak value of the velocity v'/W_m in the secondary flow boundary layer is greatly influenced by δ for the same D (or same range of κ), as shown in Figure 9; (ii) the skin friction, $\tau_{r\phi}/\tau_t$ (Figure 10), increases with and is very sensitive to the value of δ, and in addition, second maxima near the inner bend become more conspicuous. Therefore, although the

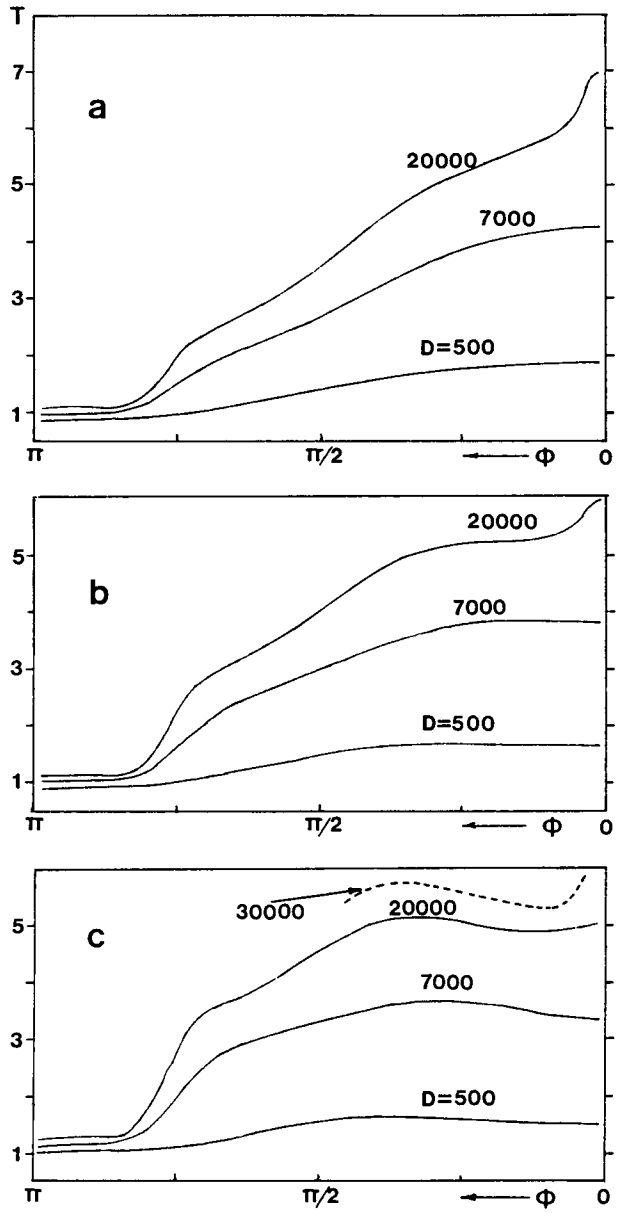

Figure 11. Total shear distribution along the wall: (a) $\delta = 0{\cdot}01$; (b) $\delta = 0{\cdot}1$; (c) $\delta = 0{\cdot}2$

assumption of very small δ for the calculation of the friction ratio is reasonable, with less than 10 per cent error for a wide range of Dean numbers, the full Navier–Stokes equations without any assumption on the value of δ must be solved to accurately determine local flow behaviour.

ACKNOWLEDGEMENT

This research was supported by the U.S. National Science Foundation under Grant MEA-8116360.

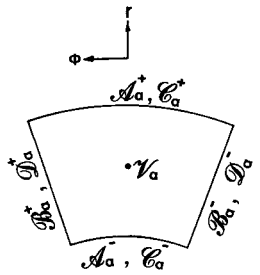

Figure 12. Boundary definition of α-cell: $\alpha = u, v, w$ or p

APPENDIX: CENTRAL-DIFFERENCE FINITE DIFFERENCE EQUATIONS

Let us define $\mathscr{A}, \mathscr{B}, \mathscr{C}, \mathscr{D}$ and $\mathscr{V}$ to be $h_2 B, h_1 B, h_2 B/h_1, h_1 B/h_2$ and $h_1 h_2 B$, respectively, which may be interpreted as the convection areas ($\mathscr{A}$ and $\mathscr{B}$), diffusion areas ($\mathscr{C}$ and $\mathscr{D}$) in the r and ϕ-directions, and the volume ($\mathscr{V}$). The symbols $\mathscr{A}_\alpha$, $\mathscr{B}_\alpha$, $\mathscr{C}_\alpha$, $\mathscr{D}_\alpha$ are defined on the α-cell boundaries with superscripts " + " and " − " (see Figure 12). The central-difference finite difference equations for (15) and (16) can be written in the staggered grid as follows.

*In the ϕ-sweep (prediction step denoted by *)*

$$\Delta u_{ij}^* + \frac{\Delta t}{\mathscr{V}_u}\left[\frac{\mathscr{B}_u^+ v_u^+ (\Delta u_{i,j+1} + \Delta u_{ij})^* - \mathscr{B}_u^+ v_u^- (\Delta u_{ij} + \Delta u_{i,j-1})^*}{2\Delta\phi} - \frac{\mathscr{D}_u^+ (\Delta u_{i,j+1} - \Delta u_{ij})^* - \mathscr{D}_u^- (\Delta u_{ij} - \Delta u_{i,j-1})^*}{R_0 \Delta\phi^2}\right] = (Ru)_{ij}, \tag{28}$$

$$\Delta v_{ij}^* + \frac{\Delta t}{\mathscr{V}_v}\left[\frac{\mathscr{B}_v^+ v_v^+ (\Delta v_{i,j+1} + \Delta v_{ij})^* - \mathscr{B}_v^- v_v^- (\Delta v_{ij} + \Delta v_{i,j-1})^*}{2\Delta\phi} - \frac{\mathscr{D}_v^+ (\Delta v_{i,j+1} - \Delta v_{ij})^* - \mathscr{D}_v^- (\Delta v_{ij} - \Delta v_{i,j-1})^*}{R_0 \Delta\phi^2}\right] + \frac{\Delta t (\Delta p_{i,j+1} - \Delta p_{ij})^*}{h_2 \Delta\phi} = (Rv)_{ij}, \tag{29}$$

$$\Delta w_{ij}^* + \frac{\Delta t}{\mathscr{V}_p}\left[\frac{\mathscr{B}_p^+ v_{ij}^n (\Delta w_{i,j+1} + \Delta w_{ij})^* - \mathscr{B}_p^- v_{i,j-1}^n (\Delta w_{ij} + \Delta w_{i,j-1})^*}{2\Delta\phi} - \frac{\mathscr{D}_p^+ (\Delta w_{i,j+1} - \Delta w_{ij})^* - \mathscr{D}_p^- (\Delta w_{ij} - \Delta w_{i,j-1})^*}{R_0 \Delta\phi^2}\right] = (Rw)_{ij}, \tag{30}$$

$$\Delta p_{ij}^* + \frac{\Delta t}{\xi \mathscr{V}_p}\left(\frac{\mathscr{B}_p^+ \Delta v_{ij}^* - \mathscr{B}_p^- \Delta v_{i,j-1}^*}{\Delta\phi}\right) = (Rp)_{ij}, \tag{31}$$

where

$$(Ru)_{ij} = \frac{\Delta t}{\mathscr{V}_u}\left[-\frac{\mathscr{A}_u^+ (u_u^+)^2 - \mathscr{A}_u^- (u_u^-)^2}{\Delta r} - \frac{\mathscr{B}_u^+ v_u^+ \cdot \text{uuw} - \mathscr{B}_u^- v_u \cdot \text{uue}}{\Delta\phi} + \frac{\mathscr{C}_u^+ (u_{i+1,j} - u_{ij})^n - \mathscr{C}_u^- (u_{ij} - u_{i-1,j})^n}{R_0 \Delta r^2} + \frac{\mathscr{D}_u^+ (u_{i,j+1} - u_{ij})^n - \mathscr{D}_u^- (u_{ij} - u_{i,j-1})^n}{R_0 \Delta\phi^2}\right]$$

$$-\frac{\Delta t}{h_1}\frac{(p_{i+1,j}-P_{ij})^n}{\Delta r}-\Delta t C_u,$$

$$(Rv)_{ij}=\frac{\Delta t}{\mathscr{V}_v}\Bigg[-\frac{\mathscr{A}_v^+ u_v^+\cdot \mathrm{vvn}-\mathscr{A}_v^- u_v^-\cdot \mathrm{vvs}}{\Delta r}-\frac{\mathscr{B}_v^+(v_v^+)^2-\mathscr{B}_v^-(v_v^-)^2}{\Delta\phi}$$
$$+\frac{\mathscr{C}_v^+(v_{i+1,j}-v_{ij})^n-\mathscr{C}_v^-(v_{ij}-v_{i-1,j})^n}{R_0\Delta r^2}+\frac{\mathscr{D}_v^+(v_{i,j+1}-v_{ij})^n-\mathscr{D}_v^-(v_{ij}-v_{i,j-1})^n}{R_0\Delta\phi^2}\Bigg]$$

$$-\frac{\Delta t}{h_2}\frac{(p_{i,j+1}-p_{ij})^n}{\Delta\phi}-\Delta t C_v,$$

$$(Rw)_{ij}=\frac{\Delta t}{\mathscr{V}_p}\Bigg[-\frac{\mathscr{A}_p^+ u_{ij}^n\cdot \mathrm{wwn}-\mathscr{A}_p^- u_{i-1,j}^n\cdot \mathrm{wws}}{\Delta r}-\frac{\mathscr{B}_p^+ v_{ij}^n\cdot \mathrm{www}-\mathscr{B}_p^- v_{i,j-1}^n\cdot \mathrm{wwe}}{\Delta\phi}$$
$$+\frac{\mathscr{C}_p^+(w_{i+1,j}-w_{ij})^n-\mathscr{C}_p^-(w_{ij}-w_{i-1,j})^n}{R_0\Delta r^2}$$
$$+\frac{\mathscr{D}_p^+(w_{i,j+1}-w_{ij})^n-\mathscr{D}_p^-(w_{ij}-w_{i,j-1})^n}{R_0\Delta\phi^2}-\Delta t C_w,$$

$$(Rp)_{ij}=\frac{-\Delta t}{\xi\mathscr{V}_p}\Bigg[\frac{\mathscr{A}_p^+ u_{ij}^n-\mathscr{A}_p^- u_{i-1}^n}{\Delta r}+\frac{\mathscr{B}_p^+ v_{ij}^n-\mathscr{B}_p^- v_{i,j-1}^n}{\Delta\phi}\Bigg].$$

Here

$$u_u^+=(u_{i+1,j}+u_{ij})^n/2, \qquad u_u^-=(u_{ij}+u_{i-1,j})^n/2$$
$$\mathrm{uuw}=(u_{i,j+1}+u_{ij})^n/2, \qquad \mathrm{uue}=(u_{ij}+u_{i,j-1})^n/2,$$
$$v_u^+=(v_{ij}+v_{i+1,j})^n/2, \qquad v_u^-=(v_{i,j-1}+v_{i+1,j-1})^n/2,$$
$$u_v^+=(u_{ij}+u_{i,j+1})^n/2, \qquad u_v^-=(u_{i-1,j}+u_{i-1,j+1})^n/2,$$
$$\mathrm{vvn}=(v_{ij}+v_{i+1,j})^n/2, \qquad \mathrm{vvs}=(v_{ij}+v_{i-1,j})^n/2,$$
$$v_v^+=(v_{ij}+v_{i,j+1})^n/2, \qquad v_v^-=(v_{ij}+v_{i,j-1})^n/2,$$
$$\mathrm{wwn}=(w_{ij}+w_{i+1,j})^n/2, \qquad \mathrm{wws}=(w_{ij}+w_{i-1,j})^n/2,$$
$$\mathrm{www}=(w_{ij}+w_{i,j+1})^n/2, \qquad \mathrm{wwe}=(w_{ij}+w_{i,j-1})^n/2,$$

C_u, C_v, C_w are the central-difference expressions of the components of **C** in (13), and the subscripts on $\mathscr{V}$ denote the appropriate volume for that variable.

In the r-sweep (correction step denoted by $n+1$)

$$\Delta u_{ij}^{n+1}+\frac{\Delta t}{\mathscr{V}_u}\Bigg[\frac{\mathscr{A}_u^+ u_u^+(\Delta u_{ij}+\Delta u_{i+1,j})^{n+1}-\mathscr{A}_u^- u_u^-(\Delta u_{ij}+\Delta u_{i-1,j})^{n+1}}{2\Delta r}$$
$$-\frac{\mathscr{C}_u^+(\Delta u_{i+1,j}-\Delta u_{ij})^{n+1}-\mathscr{C}_u^-(\Delta u_{ij}-\Delta u_{i-1,j})^{n+1}}{R_0\Delta r^2}\Bigg]$$
$$+\frac{\Delta t(\Delta p_{i+1,j}-\Delta p_{ij})^{n+1}}{h_1\Delta r}=\Delta u_{ij}^*, \tag{32}$$

$$\Delta v_{ij}^{n+1} + \frac{\Delta t}{\mathscr{V}_v}\left[\frac{\mathscr{A}_v^+ u_v^+ (\Delta v_{ij} + \Delta v_{i+1\,j})^{n+1} - \mathscr{A}_v^- u_v^- (\Delta v_{ij} + \Delta v_{i-1\,j})^{n+1}}{2\Delta r} - \frac{\mathscr{C}_v^+ (\Delta v_{i+1,\,j} - \Delta v_{ij})^{n+1} - \mathscr{C}_v^- (\Delta v_{ij} - \Delta v_{i,\,j-1})^{n+1}}{R_0 \Delta r^2}\right] = \Delta v_{ij}^*, \tag{33}$$

$$\Delta w_{ij}^{n+1} + \frac{\Delta t}{\mathscr{V}_p}\left[\frac{\mathscr{A}_p^+ u_{ij}^n (\Delta w_{ij} + \Delta w_{i+1,\,j})^{n+1} - \mathscr{A}_p^- u_{i-1,\,j}^n (\Delta w_{ij} + \Delta w_{i-1,\,j})^{n+1}}{2\Delta r} - \frac{\mathscr{C}_p^+ (\Delta w_{i+1,\,j} - \Delta w_{ij})^{n+1} - \mathscr{C}_p^- (\Delta w_{ij} - \Delta w_{i-1,\,j})^{n+1}}{R_0 \Delta r^2}\right] = \Delta w_{ij}^*, \tag{34}$$

$$\Delta p_{ij}^{n+1} + \frac{\Delta t}{\mathscr{V}_p}\left(\frac{\mathscr{A}_p^+ \Delta u_{ij}^{n+1} - \mathscr{A}_p^- \Delta u_{i-1}^{n+1}}{\Delta r}\right) = \Delta p_{ij}^*. \tag{35}$$

As can be seen in (29) and (31), v and p are coupled in the ϕ-sweep. Also, in the r-sweep, u and p (equations (32), (35)) are coupled. The resulting coupled equations lead to 2×2 block matrices in each sweep. It can be seen that ∇p and $\nabla \cdot u$ are approximated by two-point central difference relations in the momentum and continuity equations. In the ϕ-sweep, writing (31) for $j = j + 1$ and j and subtracting the latter from the former gives $\Delta p_{i,j+1}^* - \Delta p_{ij}^*$ in terms of $\Delta v_{i,j-1}^*, \Delta v_{ij}^*$ and $\Delta v_{i,j+1}^*$. If we substitute this into (29), (29) can be written in a tridiagonal form as

$$E\,\Delta v_{ij-1}^* + F\,\Delta v_{ij}^* + H\,\Delta v_{ij+1}^* = \text{RHS}. \tag{36}$$

The reader will recognize E, F, H and the RHS easily. (28) and (30) can be written in the same way as (36). A standard tridiagonal matrix solver—backward-substitution using a recurrence formula—is used for the solution of (28)–(30), then Δp_{ij}^* in (31) is obtained. Calculation procedures in the r-sweep are similar to those for the ϕ-sweep.

Finite-difference equations at the centre (or $i = 1$) can be constructed in a reasonably natural way for the staggered grid; that is, for the u-momentum, u_u^- and $\mathscr{C}_u^- (u_{ij} - u_{i-1,\,j})$ in $(Ru)_{ij}$ become $(u_0 \cos\phi + u_{1,j})^n/2$ and $\mathscr{C}_u^- (u_{1,\,j} - u_0 \cos\phi)$, respectively, and assigning to $u_0 \cos\phi$, which is u at the centre, the value at $n\Delta t$, the expressions $(\Delta u_{ij} + \Delta u_{i-1,\,j})^{n+1}$ and $\mathscr{C}_u^- (\Delta u_{ij} - \Delta u_{i-1,\,j})^{n+1}$ in (32) become Δu_{ij}^{n+1} and $\mathscr{C}_u^- \Delta u_{ij}^{n+1}$. For the v, w and p (continuity) equations we take maximum advantage of the staggered grid, for which $\mathscr{A}_v^-, \mathscr{A}_p^-, \mathscr{C}_v^-$ and $\mathscr{C}_p^-$ are exactly zero.

The finite-difference formulations described in this Appendix can be directly applied to the case with co-ordinate stretching.

REFERENCES

1. W. R. Dean, 'Note on the motion of fluid in a curved pipe', *Philos. Mag.*, **20,** 208 (1927).
2. W. R. Dean, 'The streamline motion of fluid in a curved pipe', *Philos. Mag.*, **30,** 673 (1928).
3. D. J. McConalogue and R. S. Srivastava, 'Motion of fluid in a curved tube', *Proc. R. Soc. London Ser. A*, **307,** 37 (1968).
4. A. D. Greenspan, 'Secondary flow in a curved tube', *J. Fluid Mech.*, **57,** 167 (1973).
5. W. M. Collins and S. C. R. Dennis, 'The steady motion of a viscous fluid in a curved tube', *Q. J. Mech. Appl. Math.*, **28,** 133 (1975).
6. L. R. Austin and J. D. Seader, 'Fully developed viscous flow in coiled circular pipes', *AIChE J.*, **19,** 85 (1973).
7. S. C. R. Dennis and M. Ng, 'Dual solutions for steady laminar flow through a curved tube', *Q. J. Mech. Appl. Math.*, **35,** 305 (1982).
8. W. Y. Soh and S. A. Berger, 'Laminar entrance flow in a curved pipe', *J. Fluid Mech.*, **148,** 109 (1984).
9. A. J. Chorin, 'Numerical solution of the Navier–Stokes equations', *Math. Comp.*, **22,** 745 (1968).
10. F. H. Harlow and J. E. Welch, 'Numerical calculation of time-dependent viscous incompressible flow of fluid with free surface', *Phys. Fluids*, **8,** 2182 (1965).
11. A. J. Chorin, 'A numerical method for solving incompressible viscous flow problems', *J. Comp. Phys.*, **2,** 12 (1967).
12. W. Y. Soh, 'Time-marching solution of incompressible Navier–Stokes equations for internal flow', to appear in *J. Comp. Phys.*

13. S. C. R. Dennis, 'Calculation of the steady flow through a curved tube using a new finite-difference method', *J. Fluid Mech.*, **99,** 449 (1980).
14. K. Nandakumar and J. H. Masliyah, 'Bifurcation in steady laminar flow through curved tubes', *J. Fluid Mech.*, **119,** 475 (1982).
15. H. C. Topakoglu, 'Steady laminar flows of an incompressible viscous fluid in curved pipes', *J. Math. Mech.*, **16,** 1321 (1967).
16. J. Larrain and C. F. Bonilla, 'Theoretical analysis of pressure drop in the laminar flow of fluid in a coiled pipe', *Trans. Soc. Rheol.*, **14,** 135 (1970).
17. Y. Agrawal, L. Talbot and K. Gong, 'Laser anemometer study of flow development in curved circular pipes', *J. Fluid Mech.*, **85,** 497 (1978).
18. W. Y. Soh, 'Laminar entrance flow in a curved pipe', *Ph.D. Thesis*, University of California, Berkeley, 1983.
19. S. N. Barua, 'On secondary flow in stationary curved pipes', *Q. J. Mech. Appl. Math.*, **16,** 61 (1963).